J|A|C|S
A R T I C L E S

Magnetism and Structural Chemistry of the $n = 1$ Ruddlesden−Popper Phases La_4LiMnO_8 and $La_3SrLiMnO_8$

Jonathan C. Burley,[†] Peter D. Battle,*,[†] Daniel J. Gallon,[†] Jeremy Sloan,[†]
Clare P. Grey,[‡] and Matthew J. Rosseinsky*,[§]

Contribution from the Inorganic Chemistry Laboratory, Oxford University, South Parks Road, Oxford, OX1 3QR, U.K., Chemistry Department, State University of New York at Stony Brook, Stony Brook, New York 11794-3400, and Department of Chemistry, University of Liverpool, Liverpool, L69 7ZD, U.K.

Received August 21, 2001

Abstract: Polycrystalline samples of La_4LiMnO_8 and $La_3SrLiMnO_8$ have been studied by a combination of X-ray diffraction (XRD), neutron diffraction (ND), ^{6}Li MAS NMR, electron microscopy (EM), and magnetometry. Room-temperature XRD and ND measurements suggest that both compounds have the K_2NiF_4 structure, with a disordered arrangement of Li and Mn over the six-coordinate sites. However, MAS NMR and EM demonstrate the presence of local 1:1 Li:Mn order on these sites, and EM shows that although cation order is well-developed in each *xy* sheet of corner-sharing octahedra, the sheets are stacked randomly along *z*. The structures are best described as paracrystalline, and many of the concepts of conventional crystallography are inapplicable. Magnetometry and low-temperature ND experiments show that, despite their paracrystallinity, the two compounds are ordered antiferromagnetically with susceptibility maxima at 26 and 18 K, respectively, and with ordered magnetic moments of 3.61(6) and 2.3(1) μ_B per Mn cation at 2 K. Anisotropic peak broadening reveals a 2D character in the magnetic behavior of both compounds, and $La_3SrLiMnO_8$ is well-modeled as a quadratic layer $S = {}^3/_2$ Heisenberg antiferromagnet.

1. Introduction

The magnetic properties of perovskite-related materials are often complicated by the presence of competing interaction pathways.[1] This can be true even in the lamellar Ruddlesden−Popper series, in which the quasi two-dimensional (2D) nature of the crystal structures imposes some limit on the number of interactions possible. As part of our current research into the magnetic behavior of manganese oxides, and in particular the colossal magnetoresistance phenomenon, we have embarked upon a synthetic program aimed at producing perovskite-related compounds with a limited number of well-defined superexchange pathways. Our strategy has been to introduce a second element, diamagnetic and with a chemistry different from that of Mn, onto the six-coordinate B site, the aim being to induce a pattern of cation ordering which reduces the number of significant superexchange pathways.[2−4] Here we describe the results of our attempts to synthesize two K_2NiF_4-like phases, $La_3SrLiMnO_8$ and La_4LiMnO_8, in which the B sites are occupied by lithium and manganese in a 1:1 ratio.

Li^+ differs from Mn^{3+} and Mn^{4+} in both size and charge, and the marked differences in the characteristics of the two elements might be expected to lead to some degree of chemical ordering in a 1:1 mixed $Mn^{3+/4+}$:Li^+ compound. The scheme most appropriate for 1:1 B-site ordering in a material with the K_2NiF_4 structure is a chessboard-type ordering in the *xy* plane, leading to a $\sqrt{2} \times \sqrt{2} \times 1$ expansion of the tetragonal unit cell. In the simplest case this ordering will also cause a lowering of the crystal symmetry (Figure 1) from body-centered tetragonal (*I*4/*mmm*) to A-centered orthorhombic (*Ammm*). The anion environment at the B sites in this structure is expected to lead to the electronic configurations $(t_{2g})^3(z^2)^0(x^2 - y^2)^0$ and $(t_{2g})^3(z^2)^1(x^2 - y^2)^0$ for Mn^{4+} and Mn^{3+} respectively, with the consequence that the magnetic π superexchange (Figure 2) within the *xy* plane will be strong, whereas the σ interaction will be zero in the case of Mn^{4+} and very weak in the case of Mn^{3+}. The π superexchange in the *xz* and *yz* planes will also be zero because the Li^+ cation 2s orbital has a resultant overlap integral of zero with the d_{xz} and d_{yz} orbitals of Mn. Superexchange along *z* will be weakened by the layered nature of the crystal structure and, in the case of $La_3SrLiMnO_8$, the absence of electrons in the d_{z^2} orbital. Consequently, a compound with chessboard ordering of Li and Mn would be expected to show strong antiferromagnetic coupling of nearest-neighbor Mn cations in the *xy* plane, with no other significant interactions in this plane and only weak frustrated coupling between Mn cations in neighboring planes. $La_3SrLiMnO_8$ and La_4LiMnO_8 therefore provide an opportunity to study the magnetic properties of a perovskite-related phase in which one interaction, utilizing only

---

* To whom correspondence should be addressed. E-mail: peter.battle@chem.ox.ac.uk.

[†] Oxford University.

[‡] SUNY Stony Brook. E-mail: cgrey@sbchem.sunysb.edu.

[§] University of Liverpool. E-mail: m.j.rosseinsky@liverpool.ac.uk.

(1) Cussen, E. J.; Vente, J. F.; Battle, P. D.; Gibb, T. C. *J. Mater. Chem.* **1997**, *7*, 459.

(2) Cussen, E. J.; Rosseinsky, M. J.; Battle, P. D.; Burley, J. C.; Spring, L. E.; Vente, J. F.; Blundell, S. J.; Coldea, A. I.; Singleton, J. *J. Am. Chem. Soc.* **2001**, *123*, 1111.

(3) Anderson, M. T.; Poeppelmeier, K. R. *Chem. Mater.* **1991**, *3*, 476.

(4) Battle, P. D.; Burley, J. C.; Cussen, E. J.; Hardy, G. C.; Hayward, M. A.; Noailles, L. D.; Rosseinsky, M. J. *Chem. Commun.* **1999**, *19*, 1977.

10.1021/ja012023z CCC: $22.00 © 2002 American Chemical Society

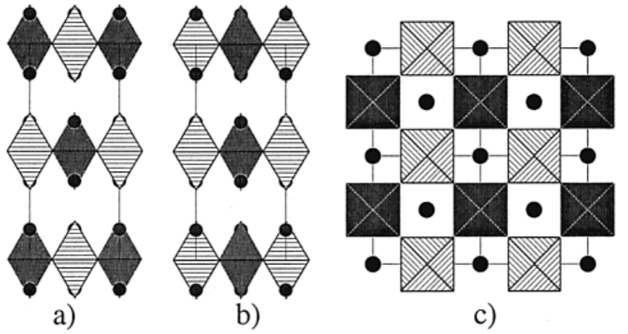

Figure 1. Idealized views of *Ammm* B-site ordered K_2NiF_4 structure type: (a) [100], (b) [010], and (c) [001] projections for 1:1 ordering are shown.

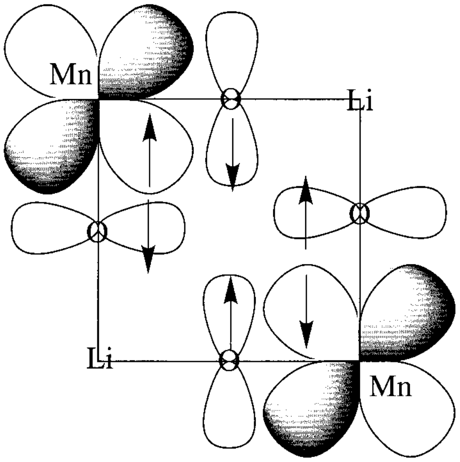

Figure 2. Electronic π-superexchange expected in 1:1 Li:Mn ordered K_2NiF_4 structure type with half-filled Mn d_{xy} orbitals.

one transition metal orbital (d_{xy}), is dominant. The results of this study were intended to provide a contrast with those obtained previously on the mixed-valence $Sr_{2-x}La_xMnO_4$ ($0 \leq x \leq 1$) system, which shows spin glass behavior over a wide composition range, with the end members being antiferromagnets.[5-8]

Both of the compounds studied in this work have been reported previously in the literature. La_4LiMnO_8 was synthesized by Abbatista and Vallino[9] and, on the basis of X-ray powder diffraction data, was described as tetragonal, with no ordering of lithium and manganese cations. $La_3SrLiMnO_8$ was reported by Demazeau et al.[10] who, in X-ray powder diffraction experiments, observed B-site ordering of the type described above. Magnetometry indicated that $La_3SrLiMnO_8$ is an antiferromagnet with a Néel temperature of 15 K; no magnetic studies were performed on La_4LiMnO_8. We were intrigued by the fact that La_4LiMnO_8 apparently did not show cation ordering, whereas $La_3SrLiMnO_8$ did, despite the similarity in ionic radii of La^{3+} and Sr^{2+}. Furthermore, the cations in several related phases[10-18] have been shown to order, either fully or partially, over these sites. The presence or absence of B-site ordering is crucial in establishing a unique magnetic interaction, and it was felt that a reinvestigation of the La/Sr/Li/Mn/O systems was warranted, especially in view of the renewed interest in layered manganates as a result of the CMR phenomenon. Accordingly, synthesis of the series $La_{4-x}Sr_xLiMnO_8$ was attempted for $0 \leq x \leq 1$, corresponding to manganese oxidation states ranging from III to IV. We show below that these phases cannot be described using conventional 3D crystallographic concepts, and that the nature of the crystal structure, together with the electron configuration of the manganese cations, leads to a magnetic behavior for $La_3SrLiMnO_8$ which approaches that of an ideal $S = {}^3/_2$ quadratic layer antiferromagnet.

2. Experimental Section

Powder samples were synthesized by standard high-temperature solid-state techniques, with the reagents being high-purity Li_2CO_3 (99.999%, Alfa), MnO_2 (99.999%, Alfa), La_2O_3 (99.999%, Alfa), and $SrCO_3$ (99.994%, Alfa) in the appropriate ratios. All were used as received, other than La_2O_3 which was dried at 800 °C prior to use. The reagents were thoroughly ground in an agate mortar before each firing. $La_3SrLiMnO_8$ could be synthesized in air. However, to produce the La_4LiMnO_8 sample (Mn^{3+}), the reagents were fired under a flow of argon in a tube furnace containing alumina boats filled with iron filings in order to minimize $p(O_2)$. This was necessary to stabilize the lower oxidation state of manganese in this phase. As a result of the low melting point of Li_2CO_3 (723 °C) and the associated high volatility, a large excess of Li_2CO_3 was used in the synthesis of these phases. After formation of the products, attempts were made to remove excess Li_2CO_3 by washing with boiling water in a Soxhlet apparatus; these led to decomposition of the main phase and were not pursued. A small excess of lithium carbonate was therefore present in the final products. Reactions were stopped when the main product phase appeared highly crystalline and the amount of Li_2CO_3 remaining was small, as indicated by X-ray powder diffraction. Preparation of samples of $La_{4-x}Sr_xLiMnO_8$ with $0 < x < 1$ was not possible using the synthetic method described above. The synthesis conditions used in the preparation of samples large enough to be studied by neutron powder diffraction were as follows: $La_3SrLiMnO_8$, 2 h 25 min at 800 °C, 14 h 45 min at 900 °C, 100% Li_2CO_3 excess used, with repeated regrinding between firings; La_4LiMnO_8, two firings under argon as described above, ramping to 900 °C at 10 °C min^{-1}, 90 min dwell at 900 °C, followed by cooling at the same rate, 200% Li_2CO_3 excess used, with regrinding between firings. La_4LiMnO_8 was synthesized as a pink-orange powder, $La_3SrLiMnO_8$ as an orange-brown powder.

X-ray powder diffraction data suitable for Rietveld analysis were collected on a Siemens D5000 X-ray powder diffractometer scanning in Bragg−Brentano geometry over the angular range $10 \leq 2\theta/° \leq 120$, $\lambda = 1.54059$ Å, $\Delta 2\theta = 0.02°$. Rietveld analyses[19] were performed using the GSAS program suite.[20] Neutron powder diffraction experiments were performed at both room temperature and 2 K on $La_3SrLiMnO_8$ and La_4LiMnO_8 using the D2B diffractometer at the Institut Laue

---

(5) Moritomo, Y.; Tomioka, T.; Asamitsu, A.; Tokura, Y.; Matsui, Y. *Phys. Rev. B* **1995**, *51*, 3297.
(6) Bouloux, J.-C.; Soubeyroux, J.-L.; Le Flem, G.; Hagenmüller, P. *J. Solid State Chem.* **1981**, *38*, 35.
(7) Bouloux, J.-C.; Soubeyroux, J.-L.; Daoudi, A.; Le Flem, G. *Mater. Res. Bull.* **1981**, *16*, 855.
(8) Kanowa, S.; Achiwa, N.; Kamegashira, N.; Aoki M. *J. Phys.* **1988**, *C8*, 829.
(9) Abbatista, F.; Vallino, M. *Atti. Accad. Sci. Torino Sect. 1* **1982**, *116*, 89.
(10) Demazeau, G.; Okhim, E. O.; Wang, K. T.; Fournes, L.; Dance, J. M.; Pouchard, M.; Hagenmüller P. *Rev. Chim. Miner.* **1987**, *24*, 183.
(11) Byeon, S. H.; Demazeau, G.; Fournes, L.; Dance, J. M.; Choy, J. H. *Solid State Commun.* **1991**, *80*, 457.
(12) Attfield, J. P.; Ferey, G. *J. Solid State Chem.* **1989**, *80*, 112.
(13) Demazeau, G.; Pouchard, M.; Zhu, L. M.; Hagenmüller, P. *Z. Anorg. Allg. Chem.* **1987**, *555*, 64.
(14) Villeneuve, G.; Rojo, T.; Demazeau, G.; Hagenmüller, P. *Mater. Res. Bull.* **1988**, *23*, 1787.
(15) Li-Ming, Z.; Demazeau, G.; Fournes, L.; Pouchard, M.; Hagenmüller, P. *C. R. Hebd. Seances Sér. II, Acad. Sci. (Paris)* **1987**, *304*, 633.
(16) Pietzuch, W.; Warda, S. A.; Massa, W.; Reinen, D. *Z. Anorg. Allg. Chem.* **2000**, *626*, 113.
(17) Warda, S. A.; Massa, W.; Reinen, D.; Hu, Z. W.; Kaindl, G.; de Groot, F. M. F. *J. Solid State Chem.* **1999**, *146*, 79.
(18) Abou-Warda, S.; Pietzuch, W.; Berghofer, G.; Kesper, U.; Massa, W.; Reinen, D. *J. Solid State Chem.* **1998**, *138*, 18.
(19) Rietveld, H. M. *Acta Crystallogr.* **1969**, *2*, 65.
(20) Larson, A. C.; Von Dreele, R. B. General Structure Analysis System (GSAS) Report LAUR 86-748, 1990.

Langevin (I.L.L.), Grenoble. The angular range $10 \leq 2\theta/° \leq 140$ was scanned with $\Delta 2\theta = 0.05°$ and $\lambda = 1.5939$ Å. The wavelength was calibrated against laboratory X-ray diffraction data.

Magic-angle-spinning (MAS) solid-state nuclear magnetic resonance experiments were performed on a CMX200 spectrometer at an operating frequency of 29.45 MHz for ^{6}Li. Spectra were acquired with a rotor-synchronized spin−echo sequence, with an evolution period of one rotor period. $\pi/2$ pulse lengths of 2.8 μs and recycle delays of 0.5 s were used. Shifts were referenced to the external reference, 1 M LiCl, at 0 ppm.

Electron diffraction patterns and high-resolution lattice images on the lithium-containing samples were collected on a JEOL 4000EX transmission electron microscope ($C_s = 1.0$ mm; point resolution = 1.6 Å) operated at 400 kV. Focal series of lattice images were obtained close to ideal Scherzer defocus conditions. Image simulations were performed using the unit cell refined from room-temperature neutron powder diffraction data and standard multislice algorithms available within the SimulaTEM (copyright A. Gomez and L. Beltran del Rio) package. The latter was used to perform simulations on large supercell fragments generated using the CrystalMaker program.

Magnetometry experiments were performed on a Quantum Design MPMS SQUID DC magnetometer, measuring both after cooling in zero field and in the applied measuring field of 100 Oe. The sample magnetization was measured as a function of applied field for both La_4LiMnO_8 and $La_3SrLiMnO_8$ at 5 and 30 K over the field range $-50 \leq H$/kOe ≤ 50.

Table 1. Refined Structural Parameters of La_4LiMnO_8 and $La_3SrLiMnO_8$ at Room Temperature and 2 K[a]

	La_4LiMnO_8		$La_3SrLiMnO_8$	
	293 K	2 K	293 K	2 K
a (Å)	3.78709(6)	3.77799(7)	3.80292(5)	3.79348(5)
c (Å)	12.9561(2)	12.9283(3)	12.6881(2)	12.6619(1)
V (Å^3)	185.818(9)	184.53(1)	183.497(7)	182.21(1)
La/Sr				
z	0.36282(7)	0.36288(7)	0.36263(6)	0.36259(6)
U_{11} (Å^2)	0.0061(4)	0.0028(3)	0.0068(3)	0.0023(3)
U_{33} (Å^2)	0.0033(4)	0.0007(4)	0.0056(4)	0.0025(4)
U_{eq} (Å^2)	0.0052(4)	0.0021(3)	0.0064(3)	0.0024(4)
Li/Mn				
U_{iso} (Å^2)	0.0109(8)	0.0074(8)	0.0098(6)	0.0064(6)
O1				
z	0.17939(9)	0.17908(9)	0.1698(1)	0.1697(1)
U_{11} (Å^2)	0.0181(6)	0.0105(6)	0.0191(6)	0.0117(5)
U_{33} (Å^2)	0.0058(7)	0.0022(7)	0.0243(7)	0.0208(7)
U_{eq} (Å^2)	0.0140(6)	0.0077(6)	0.0208(6)	0.0148(6)
O2				
U_{11} (Å^2)	0.0047(7)	0.0039(8)	0.0054(6)	0.0049(6)
U_{22} (Å^2)	0.0054(6)	0.0031(7)	0.0064(6)	0.0025(6)
U_{33} (Å^2)	0.0085(8)	0.0025(8)	0.0085(7)	0.0039(6)
U_{eq} (Å^2)	0.0062(7)	0.0031(8)	0.0068(6)	0.0038(6)
Bond Lengths (Å)				
Mn/Li−O1 × 2	2.324(1)	2.315(1)	2.154(1)	2.148(1)
Mn/Li−O2 × 4	1.89355(3)	1.88900(4)	1.90146(2)	1.89674(3)
La/Sr−O1 × 1	2.377(1)	2.376(1)	2.447(2)	2.443(1)
La/Sr−O1 × 4	2.7332(3)	2.7260(3)	2.7204(3)	2.7133(2)
La/Sr−O2 × 4	2.5970(6)	2.5905(6)	2.5794(5)	2.5739(5)

[a] All parameters determined by refinement of *I*4/*mmm* model against neutron powder diffraction data. Atomic positions: La/Sr, 4*e*, (0, 0, *z*); Li/Mn, 2*a*, (0, 0, 0), O1, 4*e*, (0, 0, *z*); O2, 4*c*, ($^1/_2$, 0, 0). Agreement indices for La_4LiMnO_8: 2 K, $\chi^2 = 4.547$, $R_{wp} = 6.48\%$, $R_p = 4.62\%$, DW-d = 0.463, 45 variables; 293 K, $\chi^2 = 3.513$, $R_{wp} = 5.86\%$, $R_p = 3.91\%$, DW-d = 0.545, 57 variables. $La_3SrLiMnO_8$: 2 K, $\chi^2 = 3.298$, $R_{wp} = 4.95\%$, $R_p = 3.77\%$, DW-d = 0.624, 58 variables; 293 K, $\chi^2 = 3.008$, $R_{wp} = 4.76\%$, $R_p = 3.63\%$, DW-d = 0.657, 56 variables.

3. Structural Chemistry

3.1. Room-Temperature X-ray and Neutron Scattering Studies. The principal phase apparent in the room-temperature X-ray powder diffraction data for $La_3SrLiMnO_8$ and La_4LiMnO_8 could be indexed using a tetragonal K_2NiF_4-type cell; the full width at half-maximum (fwhm) of the Bragg peaks was comparable to the instrumental resolution of our diffractometer ($\Delta 2\theta < 0.1°$ at $2\theta \approx 40°$). No reflections indicative of a supercell were observed, although some unreacted Li_2CO_3 was present. These data thus indicate that lithium and manganese are disordered on the B site over the length scales probed in an X-ray powder diffraction experiment. This is in contrast to the findings of Demazeau et al.,[10] who observed weak superstructure reflections for a sample of composition $La_3SrLiMnO_8$.

Rietveld analyses of laboratory X-ray data were successful (Figure S1c, Supporting Information) when a B-site disordered model, space group *I*4/*mmm* was used (La_4LiMnO_8, $\chi^2 = 1.123$, $R_{wp} = 10.04$, $R_p = 7.86$, 22 variables; $La_3SrLiMnO_8$, $\chi^2 = 1.251$, $R_{wp} = 10.45$, $R_p = 8.24$, 19 variables). Neutron powder diffraction data, collected at room temperature on the diffractometer D2B, could also be indexed in the tetragonal unit cell and could hence be accounted for in a model in which Li^+ and $Mn^{3+/4+}$ are disordered over the B sublattice. However, the neutron scattering lengths of lithium and manganese are sufficiently similar that, even if B-site ordering is present on the length scales probed by neutron diffraction, this may not have been detected in our experiments.

The lattice parameters derived from the neutron powder diffraction experiments are shown in Table 1 along with the refined atomic coordinates, atomic displacement parameters, and selected bond lengths. A Li_2CO_3 impurity phase was included in these refinements; the concentration was too low to merit inclusion in the X-ray refinements described above. The precision of the refined lattice parameters is good, and we take this, together with the instrumental fwhm of the X-ray diffraction peaks, as evidence of a tetragonal metric ($|\mathbf{a}| = |\mathbf{b}| \neq |\mathbf{c}|$) in both samples. There was no evidence of an orthorhombic distortion in any of our structure refinements, and a trial refinement using an orthorhombic model did not produce a significant improvement in the quality of the fit; the relevance of this observation will become clear below. The peak widths in both the X-ray and neutron powder diffraction experiments were as expected, given the resolution functions of the diffractometers used, and there was no evidence of anisotropic peak broadening. Trial refinements in which the occupation factors of various sites were allowed to vary showed that, despite the need to use excess Li_2CO_3 in the synthesis, the formulas $La_3SrLiMnO_8$ and La_4LiMnO_8 are accurate representations of the reaction products; all occupation factors refined to within 2σ of unity. The increase in the **c** lattice parameter on moving from $La_3SrLiMnO_8$ (Mn^{4+}) to La_4LiMnO_8 (Mn^{3+}), along with the concomitant axial elongation and equatorial contraction of the Mn/Li−O_6 octahedra, is taken to indicate that the extra electron resides in the Jahn−Teller stabilized d_{z^2} orbital. Comparison of the atomic displacement parameters (Table 1) with those of isostructural Sr_2FeO_4[21] and Sr_2VO_4[22] suggests that the values for the oxide ions in the La/Li/Mn/O systems are somewhat larger than might be expected, although the larger size of these parameters in $La_3SrLiMnO_8$ can be attributed in part to the disordered nature of the A site (La^{3+}/Sr^{2+}). The magnitude of the atomic displacement parameters changed little on cooling to 2 K. To probe the nature of this *I*4/*mmm* incoherent disorder,

---

(21) Dann, S. E.; Weller, M. T.; Currie, D. B.; Thomas, M. F.; Al-Rawwas, A. B. *J. Mater. Chem.* **1993**, *3*, 1231.

(22) Suzuki, N.; Noritake, T.; Nioki, T. *Mater. Res. Bull.* **1992**, *27*, 1171.

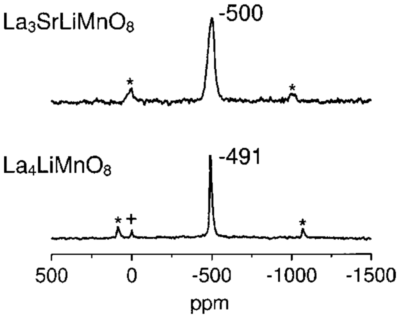

Figure 3. Magic-angle-spinning ^6Li NMR spectra of $La_3SrLiMnO_8$ and La_4LiMnO_8 acquired with spinning speeds of 15 and 17 kHz, respectively. Spinning sidebands (*) and the Li_2CO_3 resonance (+) are indicated.

nuclear magnetic resonance and electron microscopy experiments were undertaken and are reported below.

3.2. Solid-State Magic Angle Spinning ^{6}Li NMR Study. The NMR spectra of La_4LiMnO_8 and $La_3SrLiMnO_8$ both consist of a single resonance with a large negative hyperfine shift ($\delta = -491$ and -500 ppm, respectively), accompanied by spinning sidebands; a weak resonance from the Li_2CO_3 impurity is also visible (Figure 3). This is consistent with there being only one local environment for lithium in each compound, this environment being similar in the two compounds. The hyperfine shifts are extremely sensitive to the spinning speed, and thus temperature, the shift of La_4LiMnO_8 changing to -510 ppm when the spinning speed was decreased to 15 kHz. Earlier work by Lee et al.[23] showed that both the size and the sign of the hyperfine shifts in a series of lithium manganese(IV) oxides could be rationalized by considering the arrangements of the manganese ions around the lithium atoms. Furthermore, 180° Li$-$O$-$Mn(IV) interactions involving manganese e_g orbitals were predicted to result in negative hyperfine shifts (of approximately -70 to -100 ppm per Li$-$O$-$Mn interaction). Thus, to rationalize the NMR spectra of La_4LiMnO_8 and $La_3SrLiMnO_8$, the lithium local coordination environments need to be considered. Considering La_4LiMnO_8 initially, each lithium ion will be coordinated via oxide ions to 10 lanthanum ions above and below the Li/Mn planes. A random distribution of Li and Mn in the Li/Mn planes will result in five different local environments for Li which can be expressed as $Li(-O-Mn)_{4-x}(-O-Li)_x$, where $0 \leq x \leq 4$. Each Li$-$O$-$Mn interaction will result in a single discrete shift, and multiple resonances spread over more than 400 ppm are predicted on the basis of the random model. This is clearly inconsistent with the observed spectrum, where a shift close to that predicted for the local environment $Li(OMn)_4$ is observed, indicating a high degree of Li/Mn ordering within the perovskite sheets. A parallel argument can be applied in the case of $La_3SrLiMnO_8$, although the resonance is broadened (1.4 vs 0.4 kHz) by the presence of two cations (La, Sr) in the rock-salt layers. The similar shifts for both compounds are consistent with the presence of Li$-$O$-$Mn interactions involving empty $d_{x^2-y^2}$ orbitals in both systems. The observed hyperfine interaction is slightly larger than that predicted on the basis of earlier work; this is most likely due to small variations in bond lengths and bond angles between the model compounds and those studied here. This is the first direct observation of a negative hyperfine interaction involving manganese. Earlier predictions were made by considering the difference between several large positive hyperfine shifts (measured for lithium environments containing both approximately 90° and 180° interactions).

3.3. Electron Microscopy Studies. The electron diffraction patterns taken along a selection of zone axes of La_4LiMnO_8 are shown in Figure 4. The pattern shown in Figure 4a could be indexed in space group $I4/mmm$ as the [100] zone of a K_2NiF_4 structure. However, the pattern recorded for the [001] zone (Figure 4b) contains reflections that cannot be indexed in the body-centered tetragonal space group and also reflections, for example ($^1/_2$ $^1/_2$ 0), that cannot be indexed using the $\approx 4 \times 4 \times 13$ Å, K_2NiF_4-type unit cell. Instead, it is necessary to use an enlarged unit cell having $\mathbf{a}' = \mathbf{a} + \mathbf{b}$, $\mathbf{b}' = \mathbf{a} - \mathbf{b}$, and $|\mathbf{a}'| = |\mathbf{b}'| = \sqrt{2}|\mathbf{a}|$. Further complexity is apparent in the $[1\bar{1}0]$ zone of the small cell (Figure 4c), where it is clear that the reflection referred to as ($^1/_2$ $^1/_2$ 0) is not a point, but rather a rod ($^1/_2$ $^1/_2$ ξ) running parallel to $\mathbf{c}^*$. The observation of a rod of scattered intensity is characteristic of a 2D, rather than a 3D, crystal structure.

These electron diffraction patterns provide the first indication of the true structural complexity of this compound. They are consistent with a model in which cation ordering is taken to be present in the perovskite-like sheets of the K_2NiF_4 structure, but with a disordered stacking of the sheets along [001]. That is, Figure 1c is a valid description of each layer, but the stacking of the layers, although periodic in terms of separation, is not periodic in terms of site occupancy, and the structure cannot be described in space group *Ammm*. Application of the A-centering symmetry operator +(0 $^1/_2$ $^1/_2$) to the (striped) octahedron located at ($^1/_2$ 0 0) in Figure 1c would lead to the location of an identical octahedron at ($^1/_2$ $^1/_2$ $^1/_2$) and to the projections shown in Figure 1a and b. In fact, the probability that such an octahedron is centered at this site is only 0.5, with an equal probability that the other type of octahedron (shaded) is found there. Whichever type of octahedron is located at ($^1/_2$ $^1/_2$ $^1/_2$) acts as the origin for chessboard ordering in the perovskite sheet at $z = {}^1/_2$. In an alternative description, neighboring sheets of the transition metal sublattice could be said to be related by the A- or B-centering symmetry operation, but the sequence of the centring operations along [001] is random. As a consequence of this, the [100] and [010] directions of the unit cell are made equivalent, the unit cell appears to have $\mathbf{a} = \mathbf{b}$, and the symmetry is apparently tetragonal. Our model is thus based on a stacking of 2D ordered sheets which is spatially periodic but aperiodic in terms of site occupation. The relatively short length scale of the electron diffraction experiment facilitates recognition of this phenomenon, whereas X-ray powder diffraction identifies only the average, disordered, apparently tetragonal structure. The NMR experiment also recognizes the unique Li environment in the ordered planes, the coupling between neighboring sheets being negligibly small.

Further evidence for this model comes from the lattice image of La_4LiMnO_8 shown in Figure 5. In discussing this image, we shall arbitrarily assume that the circles of light contrast correspond to the lightly shaded octahedra in the structural projection drawn in Figure 1. The upper of the two *Ammm* unit cells (ca. $5 \times 5 \times 13$ Å) picked out in Figure 5 thus corresponds to the projection shown in Figure 1a. However, the lower unit

---

(23) Lee, Y. J.; Wang, F.; Grey, C. P. *J. Am. Chem. Soc.* **1999**, *120*, 12601.

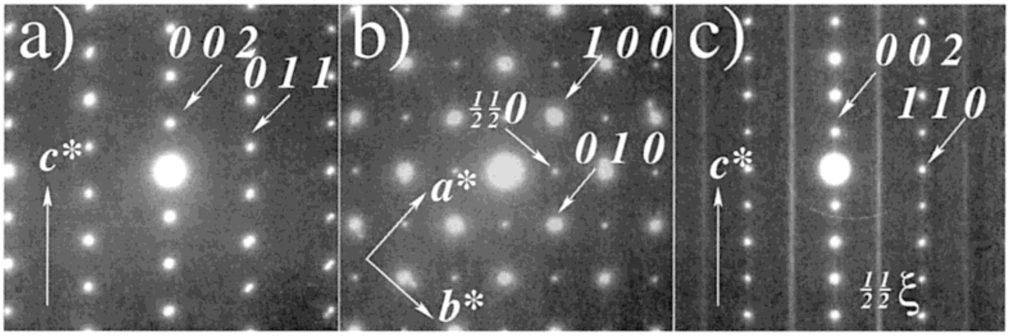

Figure 4. Electron diffraction patterns of crystallites of La_4LiMnO_8 viewed along (a) [100], (b) [001], and (c) $[1\bar{1}0]$ zone axes (K_2NiF_4 setting).

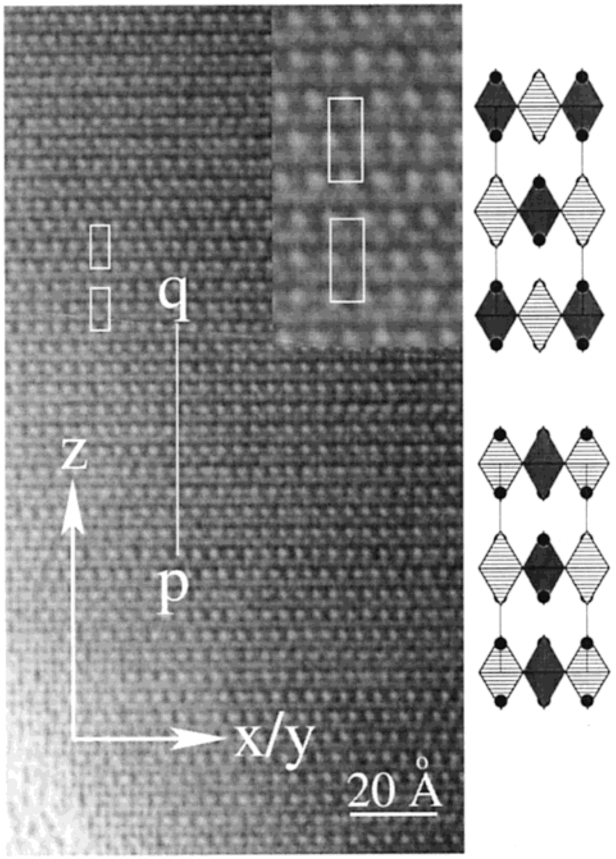

Figure 5. High-resolution electron image of La_4LiMnO_8, [100/010] orthorhombic projection. Note the lack of long-range order in *z*, as indicated by the random stacking of chessboard layers along the line pq. The inset shows the [100] and [010] projections of the *Ammm* "unit cells", with a "half-cell" between them, rendering a description in terms of conventional 3D crystallography inappropriate. Idealized [100] and [010] projections of this *Ammm* cell are shown to the right of the image for comparison.

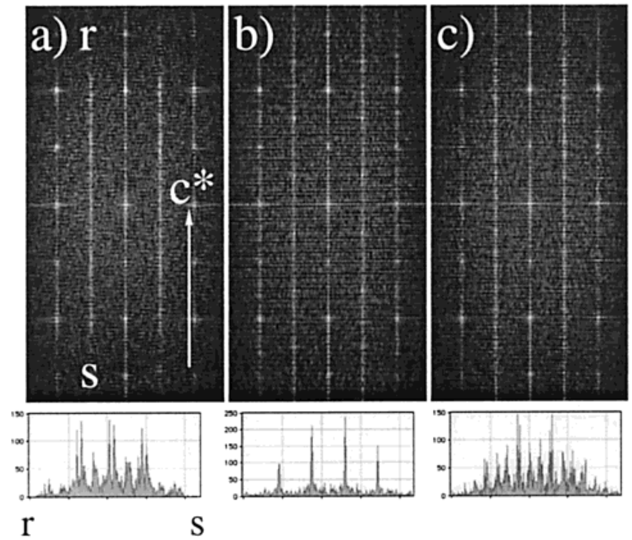

Figure 6. Fourier transforms of (a) observed lattice image, (b) same area reordered in *z*, and (c) same area with stacking randomized along *z* (selected area taken from Figure 5). The lower graph shows the intensity modulation on traveling along the line rs, which corresponds to the ($^1/_2$ $^1/_2$ ξ) reflection in Figure 4c.

cell corresponds to the projection drawn in Figure 1b. It is clear that, within a distance of $c/2 \approx 6$ Å, the viewing direction has changed from [100] to [010], or alternatively the space group has changed from *Ammm* to *Bmmm*. Inspection of the line pq, which runs parallel to *z*, reveals that this changeover occurs frequently but aperiodically and that the La sublattice is unaffected. The lattice image is thus consistent with the model of randomly stacked, ordered layers and with an electron diffraction pattern (Figure 4) which cannot be indexed in either *Ammm* or *Bmmm*. Although neutron diffraction and X-ray diffraction sample over a larger length scale and are consistent with an average tetragonal symmetry, when considering this structure on the length scale of an electron diffraction experiment it is meaningless to assign a 3D space group. The concept of a paracrystal[24,25] in which the structure along one axis is statistically determined is a more appropriate description of the Li/Mn sublattice, although the La/O sublattice can be described using conventional crystallography.

Figure 6 presents the results of a computational exercise intended to prove this point. Figure 6a is a simulated electron diffraction pattern generated by taking the Fourier transform of the experimental lattice image in Figure 5. The intensity distribution along the line rs is also illustrated. It shows a variable, nonzero intensity along the length of rs, corresponding to the ($^1/_2$ $^1/_2$ ξ) line observed in Figure 4c. When the image is edited to correspond to a periodic *Ammm* structure, the diffraction pattern which is subsequently generated (Figure 6b) contains sharp, isolated maxima along rs, as is to be expected from a crystalline material. However, when the image is edited so that the stacking sequence of the Li/Mn slabs parallel to *z* is determined by a 50:50 probability operator, the Fourier transform of the image closely resembles that calculated from the observed image. We take this as further evidence that our description in terms of paracrystallinity is valid.

---

(24) Hindeleh, A. M.; Hosemann, R. *J. Phys. C: Solid State Phys.* **1988**, *21*, 4155.

(25) Hosemann, R. *Z. Phys.* **1950**, *128*, 465.

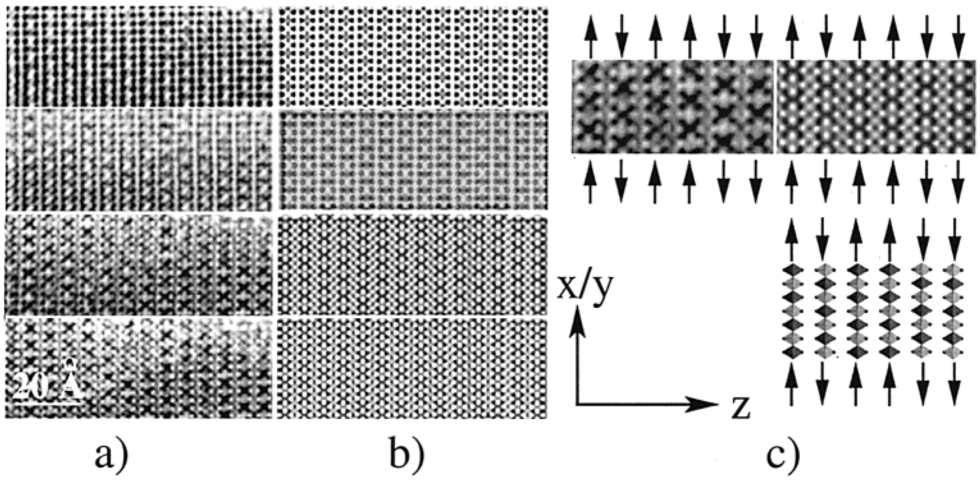

Figure 7. Focal series of $La_3SrLiMnO_8$ in orthorhombic [100/010] projection (a), with simulated images calculated for a crystal thickness of 15.5 Å and varying defocus (b). The defocus values used in the calculations are −670, −640, −600, −550, and −510 Å; the lowest of these corresponds to the lower image. An enlargement (c) of the observed and calculated images at −640 Å shows the relative shifts of the octahedra more clearly. Assigning the position of the left-most octahedron as ↑ and that of octahedra displaced by $(^1/_2\ 0\ 0)$ as ↓, the sequence of 14 octahedra along z is as follows: ↑↑↓↑↓↑↓↑↓↑↓↓↑↑. The schematic shows the relative shifts and part of the model used in the simulations.

The structural features of La_4LiMnO_8 described above are also apparent in our studies of $La_3SrLiMnO_8$. In Figure 7, we present the results of a through-focal series in the orthorhombic [100/010] projection for $La_3SrLiMnO_8$, and also the results of simulations based on the stacking sequence observed therein, using a model similar to that described above for La_4LiMnO_8. The stacking of perovskite layers again appears disordered in z. Based on the information obtained from the image simulations, the dark crosses correspond to the positions of the Mn ions, viewed in projection, and the light crosses in between correspond to the intermediate Li positions, as indicated in the enlargement and schematic representation in Figure 7c. We take the excellent agreement between observed and calculated images as evidence that the Li and Mn ions are again fully ordered in x and y in $La_3SrLiMnO_8$ and that a description in terms of random stacking of these ordered layers along z is valid.

4. Magnetic Properties

4.1. SQUID Magnetometry. Figure 8 shows the temperature dependence of the molar magnetic susceptibility of La_4LiMnO_8 and $La_3SrLiMnO_8$. Data for both samples are qualitatively similar. The susceptibility increases slowly on cooling, with a maximum occurring at 26 and 18 K for La_4LiMnO_8 and $La_3SrLiMnO_8$, respectively. Both zero-field-cooled (zfc) and field-cooled (fc) datasets overlie, with the exception of a small mismatch at low temperatures for La_4LiMnO_8. It is likely that this mismatch is intrinsic, as no paramagnetic impurities were indicated by ^6Li NMR, and an impurity in the La/Mn/O or Mn/O system might be expected to show a magnetic transition in the range $100 \leq T/K \leq 300$. These data are characteristic of antiferromagnetic ordering. The data can be described by a Curie−Weiss law above ca. 50 K, yielding Weiss constants of −48.2(2) and −28.5(2) K and Curie constants of 2.484(4) and 1.640(3) emu mol^{-1} for La_4LiMnO_8 and $La_3SrLiMnO_8$, respectively. The Curie constants are indicative of a small amount of spin−orbit coupling, with the spin-only values for Mn^{3+} and Mn^{4+} being 3.125 and 1.875, respectively. The observed larger decrease from the spin-only values for La_4LiMnO_8 is taken to reflect the greater ligand field strength associated with Mn^{4+}.

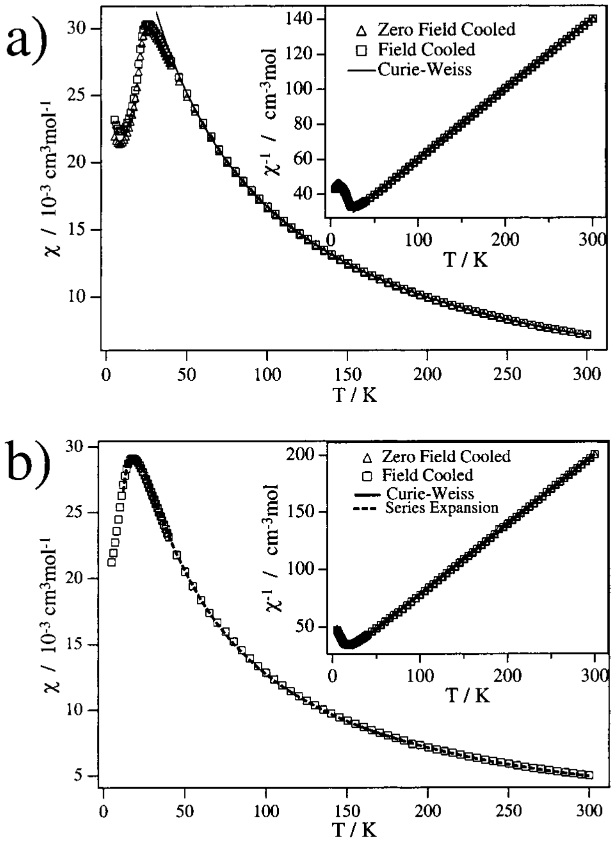

Figure 8. Temperature dependence of zfc and fc molar magnetic susceptibility and reciprocal molar susceptibility (inset) of (a) $La_3SrLiMnO_8$ and (b) $La_3SrLiMnO_8$, measured in an applied field of 100 Oe. Results of fitting a high-temperature series expansion of the quadratic layer Heisenberg model to the data in the range $60 \leq T/K \leq 300$ are shown as a dashed line in (b); the fit to a Curie−Weiss law is shown by a solid line.

Consideration of the exchange pathways in these phases, together with the electronic structure of Mn^{4+}, leads us to predict that $La_3SrLiMnO_8$ will behave as a quadratic layer Heisenberg antiferromagnet. The quadratic layer Heisenberg model has not yet been solved exactly, but approximations based on series expansions are available. The results of fitting our fc data for

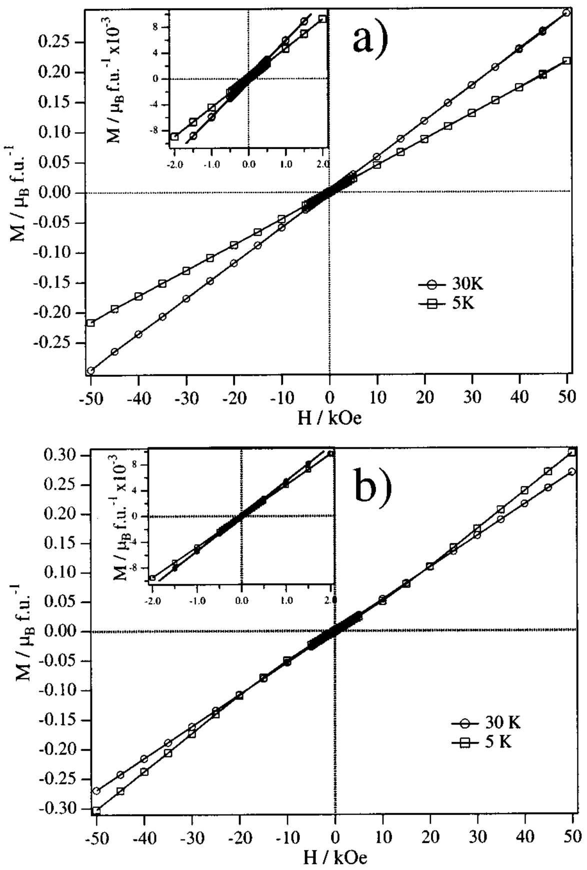

Figure 9. Magnetization (per formula unit) as a function of applied field and temperature for (a) La_4LiMnO_8 and (b) $La_3SrLiMnO_8$.

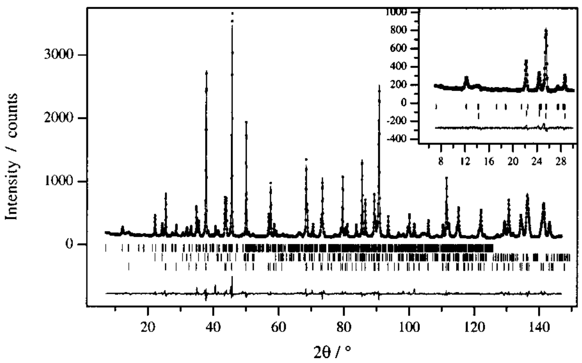

Figure 10. Observed (●), calculated (—), and difference neutron powder diffraction profiles from La_4LiMnO_8 at 2 K; the low-angle (magnetic) scattering is magnified in the inset. The upper set of tic marks indicate magnetic reflections, the middle set indicate reflections from Li_2CO_3, and the lower set are from the main structural phase.

$La_3SrLiMnO_8$ to such a model,[26] which is valid in the high-temperature region, are shown in Figure 8b. The fit for $60 \leq T/K \leq 300$ is of good quality, yielding values of $Jk = 5.2$ K and $g = 1.93$. It should be noted that, although the maximum at ca. 18 K is well-fitted by the model, the maximum itself is not included in the temperature range fitted. This observation lends weight to the proposition that the behavior of $La_3SrLiMnO_8$ is that of an ideal $S = {}^3/_2$ quadratic layer Heisenberg system. The results of fitting the susceptibility of La_4LiMnO_8 to this model were much less satisfactory. We attribute this to the partial occupancy of the d_{z^2} orbital and the consequent increase in the anisotropy for the Mn^{3+} cation.

The magnetization of both samples was measured as a function of field ($-50 \leq H/\text{kOe} \leq 50$) at 5 and 30 K (Figure 9). No hysteresis was apparent in either measurement. For applied fields of $-2 \leq H/\text{kOe} \leq 2$ (inset), both samples show a lower magnetization at 5 K than at 30 K, as expected given the susceptibility maxima apparent in Figure 8. For an applied field greater than ca. 7.5 ± 2.5 kOe, the susceptibility of $La_3SrLiMnO_8$ as determined by $\partial M/\partial H$ becomes greater at 5 K than at 30 K. The increase in susceptibility leads to a higher magnetization at 5 K than at 30 K for an applied field greater than 17.5 ± 2.5 kOe. The susceptibility of La_4LiMnO_8 at 5 K is always less than that at 30 K. These data are taken to indicate that La_4LiMnO_8 is antiferromagnetic for applied fields of $-50 \leq H/\text{kOe} \leq 50$ (the measuring limit of the magnetometer used in this study) and that $La_3SrLiMnO_8$ is antiferromagnetic for applied fields of ca. $-15 \leq H/\text{kOe} \leq 15$. A possible interpretation of the data for $La_3SrLiMnO_8$ in fields stronger than ca. 7.5 kOe is that a spin-flop occurs at high field values. This has been observed previously in studies of other low-dimensional systems with spherical ions, for example the d^5 systems $BaMnF_4$ and $(CH_3NH_3)_2MnCl_4$.[27,28] This spin-flop transition does not occur in the d^4 compound La_4LiMnO_8 because the energy barrier for spin reorientation is higher due to the stronger anisotropy of the d^4 ion. Neutron diffraction measurements in large applied fields would be of interest to investigate this issue further.

4.2. Low-Temperature Neutron Diffraction. On cooling from room temperature to 2 K, extra low-angle Bragg peaks, which could not be indexed using a ca. 4 × 4 × 13 Å K_2NiF_4 cell, appeared in the neutron powder diffraction patterns of both La_4LiMnO_8 and $La_3SrLiMnO_8$. They could be indexed in a $2a \times 2a \times c$ K_2NiF_4 cell, the two strongest new reflections being 100 and 101. However, although the profile of the 100 peak was similar to those observed at room temperature, the 101 peak was very broad and somewhat asymmetric. These data support the hypothesis that both compounds show long-range magnetic order at low temperatures, albeit with some anisotropic character in the magnetic structure. The diffraction patterns of both compounds could be accounted for (Figure 10) using a model which comprised the Li_2CO_3 impurity phase, a structural component essentially identical to that observed at room temperature, and a contribution from an antiferromagnetic spin arrangement on the Mn sublattice. The latter component was described in a $2a \times 2a \times c$ unit cell, the distribution and spin ordering of the Mn cations in the *xy* plane being as shown in Figure 2. Thus, the Mn/Li cation ordering in these layers is revealed by the magnetic neutron scattering, even though it is not apparent in the nuclear scattering. It was necessary to include in the refinements a parameter to describe the anisotropic Scherrer broadening of the *hkl* magnetic reflections relative to *hk*0. This broadening reflects the lack of order along [001]. It can be shown that the magnetic structure factor ${}^{mag}F_{100}$ depends only on the magnetic structure within the well-ordered *xy* planes, and structural disorder along *z* therefore does not prevent the 100 reflection appearing as a sharp Bragg peak. However, the 101 reflection does require periodicity along *z* in order for ${}^{mag}F_{101}$ to be well-defined, and the disorder therefore crucially

---

(26) Lines, M. E. *J. Phys. Chem. Solids* **1970**, *31*, 101.

(27) van Amstel, W. D.; de Jongh, L. J. *Solid State Commun.* **1972**, *11*, 1423.

(28) Holmes, L.; Eibschütz, M.; Guggenheim, H. J. *Solid State Commun.* **1969**, *7*, 973.

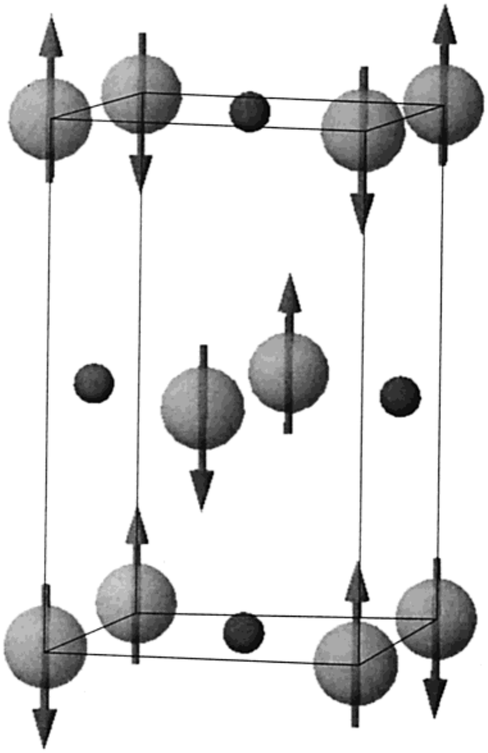

Figure 11. Schematic of part of the magnetic structure of La_4LiMnO_8 and $La_3SrLiMnO_8$. Li and Mn ions only are shown for clarity. Each *xy* layer possesses long-range order, but the layers do not couple along *z*. The structural unit cell shown is a $\sqrt{2} \times \sqrt{2} \times 1$ expansion of the basic tetragonal cell. Note that long-range 3D order is not thought to be present.

reduces the size of the coherent regions contributing to this reflection, causing it to broaden to the point where it could arguably be described as a maximum in the diffuse scattering rather than as a Bragg peak. Unfortunately, the quality of our data preclude an accurate determination of the effective particle size by Warren's method.[29] Our data analysis was insensitive to the choice of magnetic propagation vector along *z*, provided that the nearest-neighbor spins on a chess-board ordered Li/Mn array were coupled antiferromagnetically in each of the *xy* layers. A Rietveld analysis then yielded the structural parameters listed in Table 1, with ordered magnetic moments of 3.61(6) and 2.3(1) μ_B per Mn cation for La_4LiMnO_8 and $La_3SrLiMnO_8$, respectively. The observed reduction from the spin-only values (4 and 3 μ_B) can be attributed to the effect of covalency, which would be expected to be more significant in the case of the Mn^{4+} compound. The ordered magnetic moments were found to lie along *z*, although the quality of our data does not allow us to rule out a small amount of spin canting. We note that the observation of a highly disordered magnetic structure in *z* supports the proposal that La_4LiMnO_8 and $La_3SrLiMnO_8$ can be described as 2D magnetic systems.

Part of the magnetic structure proposed for both La_4LiMnO_8 and $La_3SrLiMnO_8$ is drawn in Figure 11. It can be seen that the magnetic interactions between adjacent *xy* sheets are frustrated, and this, together with the paracrystalline nature of the structure, leads to the weakening of exchange interactions along *z*. As noted, this effect is expected to be greater for $La_3SrLiMnO_8$ due to the presence of an empty d_{z^2} orbital on Mn^{4+}.

5. Conclusion

The cation ordering and magnetic behavior observed in these two K_2NiF_4-like phases is much more complex than that described recently in the case of the perovskite $LaMn_{1-x}Li_xO_3$.[30] The transition metal centers in both $La_3SrLiMnO_8$ and La_4LiMnO_8 interact magnetically in a manner which can be accounted for on the basis of a superexchange mechanism involving the d_{xy} orbitals of manganese and the oxygen p_π orbitals. This provides an unusual example of one-orbital transition metal chemistry and is expected to serve as a model for studies of magnetic interactions in perovskites. The hyperfine exchange between manganese and lithium ions observed in the NMR experiment likewise utilizes a single Mn orbital, the empty $d_{x^2-y^2}$, on this occasion coupling to the empty Li 2s orbital via an oxide $2p_\sigma$ orbital. Thus, the π and σ interactions in these materials have been studied separately, the former through magnetometry and low-temperature neutron powder diffraction and the latter through ^{6}Li NMR. These systems provide the first experimental evidence of a negative hyperfine shift in Li:Mn systems and validate the proposed mechanisms for such shifts.

The structures of both La_4LiMnO_8 and $La_3SrLiMnO_8$ cannot be described by conventional crystallographic techniques due to the lack of long-range structural order. Rather, a two-subcell approach is required, using the paracrystal formalism in which translation and symmetry operators are coupled with a probability operator. The application of this concept of paracrystallinity allows these materials to be described as single, homogeneous compounds, whereas the standard approach of normal space group crystallography is unable to account successfully for the highly unusual structural features identified in this study. X-ray methods are not suitable for the adumbration of structures possessing complete but incoherent cation ordering, because the coherence length of X-rays is greater than the structural coherence length along *z*. However, the incoherence of the ordered electron spins along *z* does not cause a collapse of the magnetic Bragg peaks; rather, the *hk*0 peaks due to the magnetic ordering clearly show the presence of long-range *xy* cation ordering on the B site, both structural and magnetic. This complete cation ordering is also well illustrated by the use of NMR, which probes local chemical environment, and electron microscopy, which allows us to observe the structural complexities at close to the atomic level.

The results of both neutron diffraction and magnetometry are consistent with the classification of these compounds as 2D antiferromagnets, as predicted by a consideration of the magnetic coupling routes available to the Mn cations. The evidence to support this conclusion is provided by the unusual *hkl*-dependent line broadening seen in the low-temperature neutron diffraction patterns and the good quantitative agreement over a wide temperature range, including $T(\chi_{max})$, between the observed and calculated susceptibilities of $La_3SrLiMnO_8$. We note that in 2D systems such as these, $T(\chi_{max})$ does not necessarily coincide with the Néel temperature, below which long-range magnetic ordering occurs. In these remarkable compounds, the coincidence of paracrystallinity along [001] and cation ordering within the *xy* planes generates a wealth of fascinating structural chemistry and magnetism.

---

(29) Warren, B. E. *Phys. Rev.* **1941**, *59*, 693.

(30) Gönen, Z. S.; Gopalakrishnan, J.; Sirchio, S. A.; Eichhorn B. W.; Smolyaninova, V.; Greene, R. L. *J. Solid State Chem.* **2001**, *159*, 59.

Acknowledgment. The authors thank Thomas Hansen and Young Joo Lee for experimental assistance at the I.L.L., Grenoble, and with the NMR experiments, respectively. C.P.G. thanks the NSF for support via DMR0074858, J.S. is grateful to the Royal Society for a Research Fellowship, and J.C.B., P.D.B., D.J.G., and M.J.R. thank EPSRC for funding.

Supporting Information Available: Figure of observed, calculated, and difference neutron powder diffraction profiles (PDF). This material is available free of charge via the Internet at http://pubs.acs.org.

JA012023Z